



**HAL**  
open science

## InP double heterojunction bipolar transistors for terahertz computed tomography

Dominique Coquillat, Alexandre Duhant, Meriam Triki, Virginie Nodjiadjim, Agnieszka Konczykowska, Muriel Riet, Nina Dyakonova, Olivier Strauss, Wojciech Knap

### ► To cite this version:

Dominique Coquillat, Alexandre Duhant, Meriam Triki, Virginie Nodjiadjim, Agnieszka Konczykowska, et al.. InP double heterojunction bipolar transistors for terahertz computed tomography. AIP Advances, 2018, 8, pp.#085320. 10.1063/1.5039331 . hal-01900570

**HAL Id: hal-01900570**

**<https://hal.science/hal-01900570>**

Submitted on 6 Jun 2019

**HAL** is a multi-disciplinary open access archive for the deposit and dissemination of scientific research documents, whether they are published or not. The documents may come from teaching and research institutions in France or abroad, or from public or private research centers.

L'archive ouverte pluridisciplinaire **HAL**, est destinée au dépôt et à la diffusion de documents scientifiques de niveau recherche, publiés ou non, émanant des établissements d'enseignement et de recherche français ou étrangers, des laboratoires publics ou privés.



Distributed under a Creative Commons Attribution 4.0 International License

# InP double heterojunction bipolar transistors for terahertz computed tomography

Cite as: AIP Advances **8**, 085320 (2018); <https://doi.org/10.1063/1.5039331>

Submitted: 07 May 2018 . Accepted: 30 July 2018 . Published Online: 27 August 2018

Dominique Coquillat, Alexandre Duhant, Meriam Triki, Virginie Nodjiadjim, Agnieszka Konczykowska, Muriel Riet, Nina Dyakonova, Olivier Strauss, and Wojciech Knap



View Online



Export Citation



CrossMark

## ARTICLES YOU MAY BE INTERESTED IN

[Electrically controlled wire-channel GaN/AlGaN transistor for terahertz plasma applications](#)  
Applied Physics Letters **112**, 133502 (2018); <https://doi.org/10.1063/1.5023391>

[Tutorial: Terahertz beamforming, from concepts to realizations](#)  
APL Photonics **3**, 051101 (2018); <https://doi.org/10.1063/1.5011063>

[Indium antimonide detector for spectral characterization of terahertz sources](#)  
Journal of Applied Physics **123**, 064502 (2018); <https://doi.org/10.1063/1.5002765>

AVS Quantum Science

Co-published with AIP Publishing



Coming Soon!

## InP double heterojunction bipolar transistors for terahertz computed tomography

Dominique Coquillat,<sup>1,a</sup> Alexandre Duhant,<sup>2,3</sup> Meriam Triki,<sup>2</sup>  
Virginie Nodjiadjim,<sup>4</sup> Agnieszka Konczykowska,<sup>4</sup> Muriel Riet,<sup>4</sup>  
Nina Dyakonova,<sup>1</sup> Olivier Strauss,<sup>3</sup> and Wojciech Knap<sup>1</sup>

<sup>1</sup>Laboratoire Charles Coulomb (L2C), University of Montpellier, CNRS, Montpellier, France

<sup>2</sup>Department of Research and Development, T-Waves Technologies, Montpellier, France

<sup>3</sup>Laboratoire d'Informatique, de Robotique et de Microélectronique de Montpellier (LIRMM), University of Montpellier, CNRS, Montpellier, France

<sup>4</sup>III-V Lab, Campus de Polytechnique, 1 Avenue Augustin Fresnel, Palaiseau, France

(Received 7 May 2018; accepted 30 July 2018; published online 27 August 2018)

We present experimental studies of terahertz radiation detection by InP double heterojunction based transistors. We analyze the relation between their static characteristics and the experimentally determined voltage and current responsivities, showing importance of internal device parasitic capacitances and the external circuit loading effects. Finally, we demonstrate the use of these transistors for terahertz radiation computed tomography leading to 3D visualization of concealed objects. Our results pave the way towards wide use of heterojunction based transistors for terahertz imaging. © 2018 Author(s). All article content, except where otherwise noted, is licensed under a Creative Commons Attribution (CC BY) license (<http://creativecommons.org/licenses/by/4.0/>). <https://doi.org/10.1063/1.5039331>

### I. INTRODUCTION

Nowadays high frequency electronics uses two distinct families of transistors: field effect transistors and heterojunction based transistors (HBTs). They compete reaching impressive cut off frequencies going up to terahertz (THz) range. Except their usual functions related to switching and amplifying of voltage or current, both have been demonstrated as efficient direct THz radiation detectors.<sup>1–8</sup> Actually, both types of the transistors have shown that once equipped with antennas, they can capture THz radiation from the open space, rectify it, and deliver the voltage or current proportional to incoming THz radiation power. The most of the works were dedicated to the field effect transistors that rectify THz radiation by plasma related nonlinearities.<sup>9,10</sup> After pioneering works of Al Hadi *et al.*<sup>5</sup> and Vassilev *et al.*<sup>6</sup> only very small attention was devoted to HBTs.

The importance of HBTs comes also from the fact that many companies are using this technology for optical fiber transmission systems.<sup>11</sup> Therefore, the studies of the THz detection by HBT is crucial to extend the high data-rate capacity of optical fiber transmission to THz wireless systems.

In this work, we present experimental studies of THz detection by InP double heterojunction based transistors (DHBTs),<sup>12</sup> in a mode where only the emitter-base junction of DHBT rectifies THz radiation and collector-base junction is unbiased (so called passive mode). We analyse the relation between the static DHBT characteristics and the experimentally determined responsivities, showing importance of internal device parasitic capacitances and the external circuit loading effects. We demonstrate DHBT THz imaging capabilities in the experiments of computed tomography showing an efficient 3D imaging of concealed objects.

---

<sup>a</sup>dominique.coquillat@umontpellier.fr

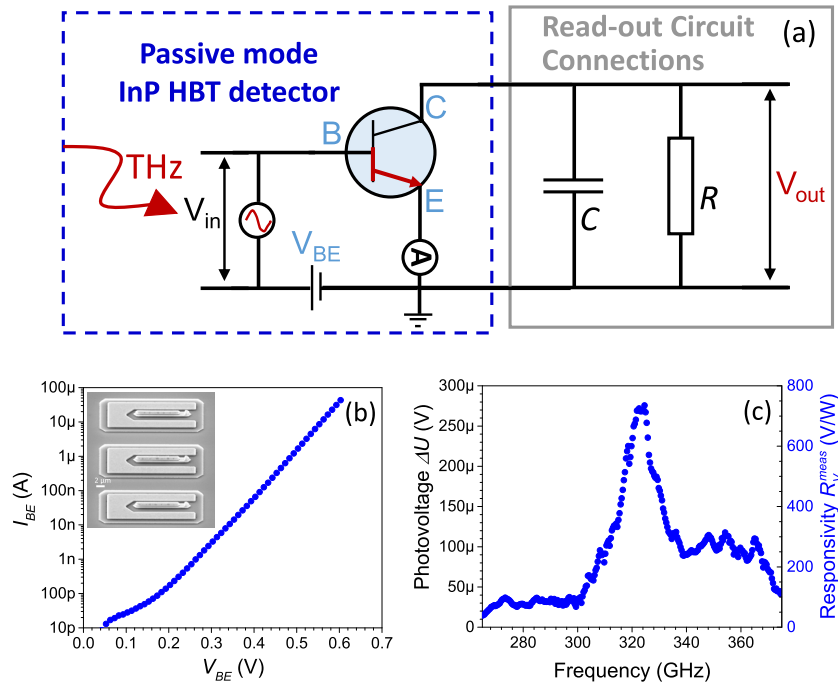


FIG. 1. (a) Schematic of the InP DHBT THz detector and read-out circuit connections. (b) Input characteristics  $I_{BE} - V_{BE}$  of the 3-finger device. Inset: SEM photograph of a 3-finger DHBT with  $3 \times 10 \mu\text{m} \times 0.7 \mu\text{m}$  emitter area. (c) Photo-voltage  $\Delta U$  (left hand scale) and area normalized voltage responsivity  $R_V^{meas}$  (right hand scale) as a function of frequency for  $V_{BE} = 0.43$  V.

## II. DEVICES

The THz detectors were fabricated using InP double HBT technologies. The investigated devices were multi-finger devices formed using three equally spaced parallel single-transistor fingers and with an active emitter area of  $3 \times 10 \times 0.7 \mu\text{m}$ . The measurement circuit and the base-emitter  $I_{BE} - V_{BE}$  characteristics of one of the 3-finger devices are shown in Fig. 1(a) and 1(b) for the collector connected to the high impedance read-out circuit. For all devices the current gain cutoff frequency ( $f_T$ ) and the power gain cutoff frequency ( $f_{max}$ ) were above 280 GHz. The static current gain was around 40 and the common-emitter breakdown voltage was above 5 V. More details about the epitaxial process, relevant layout dimensions and device parameters can be found in Ref. 12. For THz experiments the substrate was thinned down to  $d \sim 160 \mu\text{m}$  and the devices were mounted in gold plated ceramic chip carriers. The incoming THz radiation was coupled to the devices via the contact pads and/or the coupling wires playing the role of the antennas.<sup>13</sup> We have evaluated the room temperature detection performances of the devices in the sub-THz range from 265 GHz up to 375 GHz. The typical photo-voltage versus frequency result is shown in Fig. 1(c).

## III. THz RESPONSIVITY MEASUREMENTS

The InP DHBTs were connected in the common-emitter configuration. In this configuration the rectification is related to the emitter-base (n-p) junction current-voltage characteristics nonlinearity as described in Ref. 6. Unlike the two-terminal passive detector case presented in Ref. 6, the collector was not kept open, but connected to the read-out circuit, as shown in Fig. 1(a). The incident radiation was modulated by a chopper, and the photo-voltage  $\Delta U$  was measured using a standard lock-in technique with a voltage preamplifier 10 M $\Omega$  input resistance. The Figure 1(c) shows the photo-voltage  $\Delta U$  induced by the radiation in the 265 - 375 GHz frequency range at a base-emitter bias of  $V_{BE} = 0.43$  V and the area-normalized voltage responsivity  $R_V^{meas}$  (right hand scale).

The voltage responsivity in V/W was extracted from  $\Delta U$  using the relation:

$$R_V^{meas} = (\Delta U S_t) / (P_t S_a), \quad (1)$$

where  $P_i$  is the power of the incoming radiation in the focal plane of the device.  $S_i = \pi d^2/4$  is the radiation beam spot area, and  $S_d$  is the total area of the device which includes contact pads ( $240 \mu\text{m} \times 350 \mu\text{m}$ ). There is a sharp responsivity maximum around 322 GHz, with a peak value of 0.7 kV/W, that we attribute to the presence of contact pad antenna resonance or/and substrate standing wave phenomena. This is because the InP substrate and layers act as an over-sized dielectric resonator structure, and the detection is determined by the electromagnetic field distribution subjected to the thickness and dimensions of the substrate and to the rectangular metal pads dimensions.

The  $I_{BE}$  current was also measured using a Keithley Source Meter unit, while keeping the collector connected to the lock-in read-out circuit. This way the current response was obtained as difference of  $I_{BE}$ , with and without THz radiation illumination. The Figure 2(a) shows photo-current

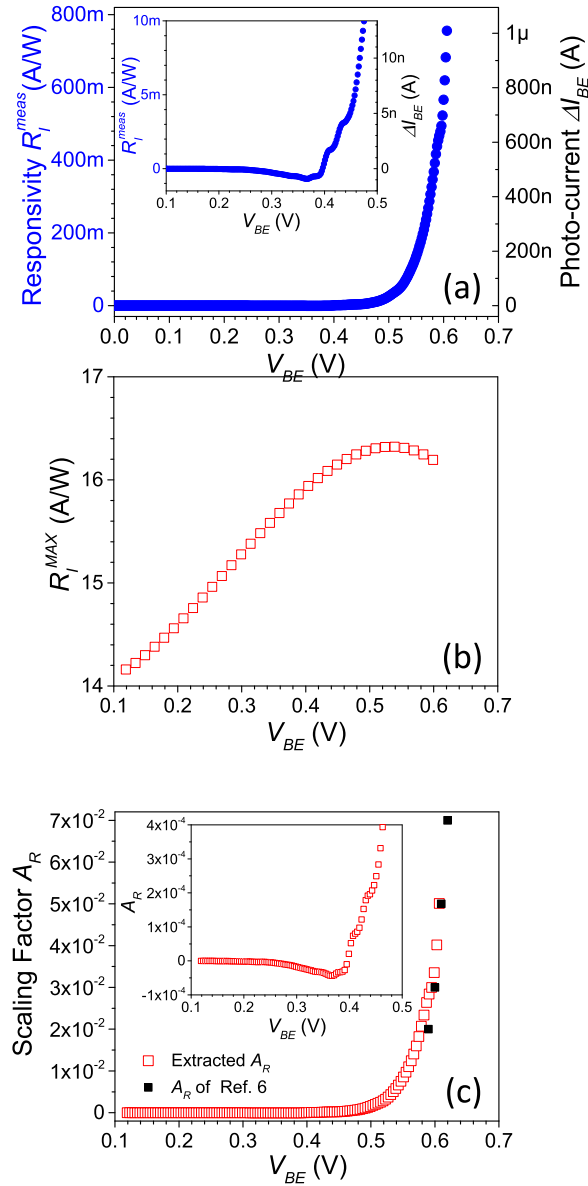


FIG. 2. (a) Measured photo-current  $\Delta I_{BE}$  (right hand scale) and area-normalized current responsivity  $R_I^{meas}$  (left hand scale) at 322 GHz. Inset: Enlarged fragment of  $\Delta I_{BE}$  dependence. (b) Maximum theoretical responsivity  $R_I^{MAX}$  estimated from Eq. (2). (c) Extracted scaling factor dependence  $A_R$  from the maximum theoretical responsivity and measured current responsivity (open red square curve). Comparison with estimated  $A_R$  of Ref. 6 (full black square curve). Please note that  $A_R$  was called  $C_R$  in Ref. 6. Inset: Enlarged fragment of  $A_R$  dependence.

$I_{BE}$  induced by 322 GHz radiation (right hand scale) and the area-normalized current responsivity  $R_I^{meas}$  (left hand scale), normalized in the same way than  $R_V^{meas}$ . The current responsivity in A/W increases in the whole investigated  $V_{BE}$  range except in the narrow 0.3 - 0.4 V range, where the weak decrease can be visualized in the inset of Fig. 2(a).

To analyse observed  $V_{BE}$  dependences of the current responsivity, we follow an approach of Ref. 6. We calculate the maximum theoretical current responsivity  $R_I^{MAX}$  from standard microwave detector theory<sup>14</sup> as:

$$R_I^{MAX} = \frac{1}{2} \frac{d^2 i_{BE}}{dV_{BE}^2} \left/ \left( \frac{di_{BE}}{dV_{BE}} \right) \right., \quad (2)$$

where  $v_{BE}$  is the induced voltage at the THz frequency and  $i_{BE}$  is the generated current around the detector operating point. We calculate the first and the second derivative from the measured  $I_{BE}-V_{BE}$  characteristics. The resulting calculated maximum responsivity  $R_I^{MAX}$  is plotted in Fig. 2(b). The theoretical current responsivity is in the order of 10 A/W. This is the same order of magnitude as predicted for FET based THz detectors.<sup>15</sup>

The  $R_I^{MAX}$  shape and amplitude are very different from the experimental ones. In fact, when comparing Figs. 2(a) and 2(b) one can see that experimental responsivity is in the range of (mA/W) and the theoretical one is in the range of (A/W). This huge difference is explained by the parasitic coupling that depends on the junction polarization. Therefore it is represented by the scaling factor  $A_R$  shown in Fig. 2(c). The main reason of this reduction of the responsivity is the base-emitter capacitance  $C_{BE}$  that short-circuits incoming THz signal. The scaling factor dependence  $A_R$  vs  $V_{BE}$  can be determined as the ratio of  $R_I^{MAX}$  plotted in Fig. 2(b) and the measured current responsivity  $R_I^{meas}$  shown in Fig. 2(a). The scaling factor dependence is illustrated in Fig. 2(c). One can observe that indeed, this factor reduces the THz rectification efficiency by two orders of magnitude or more. Improvement of this factor by reduction of  $C_{BE}$  is the key point to improve the THz responsivity of DHBT detectors. We would mention also that the obtained scaling factor values are of the same order of magnitude as those calculated numerically for similar devices in Ref. 6 and represented by the full black squares in Fig. 2(c).

The voltage responsivity (measured by the Lock-in technique at the collector terminal) for 322-GHz radiation is shown in Fig. 3(a). One can see that the voltage responsivity first increases with  $V_{BE}$ , but later saturates at  $\sim 0.43$  V, and decreases slightly. The voltage responsivity behavior is different from the current responsivity one.

The maximum theoretical voltage responsivity can be estimated from the  $I_{BE}-V_{BE}$  characteristics as:

$$R_V^{MAX} = \frac{1}{2} \frac{d^2 i_{BE}}{dV_{BE}^2} \left/ \left( \frac{di_{BE}}{dV_{BE}} \right)^2 \right., \quad (3)$$

The expected real voltage responsivity  $R_V$  is scaled by  $A_R$  in the same way the current responsivity one.<sup>6</sup> However  $R_V$  is scaled, in addition, by the impedance mismatch between the detector and the read-out circuit – loading effect.<sup>16-19</sup> Therefore, expected voltage responsivity  $R_V$  should be estimated as:

$$R_V = \left[ \frac{1}{2} \frac{d^2 i_{BE}}{dV_{BE}^2} \left/ \left( \frac{di_{BE}}{dV_{BE}} \right)^2 \right. \right] \times A_R \times A_{Load}, \quad (4)$$

where  $A_{Load}$  is an additional read-out circuit connections dependent factor (loading factor). It depends on  $V_{BE}$  through  $R_{BE}$ . Using simple voltage divider approach we can write  $A_{Load}$  as:

$$A_{Load} = \frac{1}{1 + R_{det}/Z_L}, \quad (5)$$

where  $R_{det}$  is the sum of the emitter-base resistance  $R_{BE}$  and the base-collector resistance  $R_{BC}$ . The load impedance  $Z_L$  of the external circuit [Fig. 1(a)] can be written as

$$\frac{1}{Z_L} = \frac{1}{R} + i\omega_{mod}C, \quad (6)$$

where  $R$  is the resistance of the pre-amplifier (10 M $\Omega$ ),  $C$  is the capacitance of the cables between the DHBT and the pre-amplifier,  $\omega_{mod}$  is the modulation frequency of the incident THz radiation. The

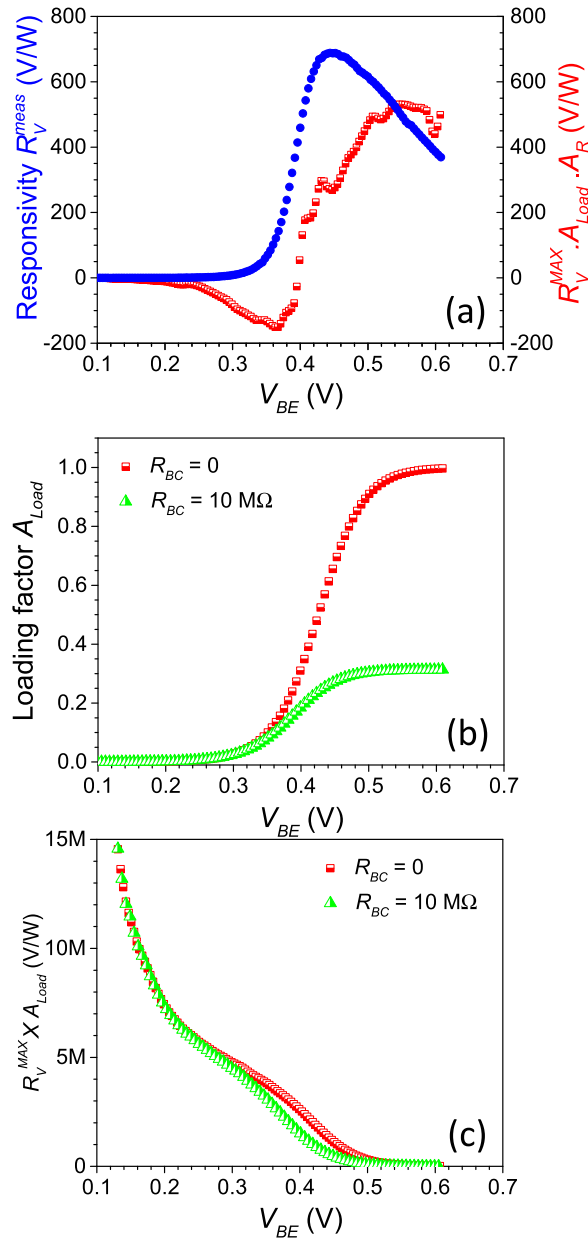


FIG. 3. (a) area-normalized voltage responsivity  $R_V^{meas}$  at 322 GHz (blue dot curve, left hand scale) and expected voltage responsivity scaled by the loading effect  $A_{Load}$  (for  $R_{BC} = 10$  M $\Omega$ ) and the scaling factor  $A_R$  (red square curve, right hand scale). (b) Loading factor  $A_{Load}$  for two different  $R_{BC}$  values (0 and 10 M $\Omega$ ). (c)  $R_V^{MAX}$  attenuated by the loading effect only, for  $R_{BC} = 0$  and 10 M $\Omega$ .

load impedance  $Z_L$  was estimated to be  $\sim 4.6$  M $\Omega$  at  $\omega_{mod} = 619$  Hz. To illustrate the contribution of the base-collector resistance in the loading factor, Fig. 3(b) shows  $A_{Load}$  for two different values of  $R_{BC}$ . For large  $V_{BE}$  voltage,  $R_{BE}$  is small and loading factor  $A_{Load}$  is dominated by the value of  $R_{BC}$ . At small  $V_{BE}$  voltages,  $R_{BE}$  is large and the curves for different  $R_{BC}$  tend to coincide. Fig. 3(c) shows the results of  $R_V^{MAX} \times A_{Load}$  calculations.

One can see that the loading effect alone can not explain the  $V_{BE}$  dependence of the voltage responsivity. Results of calculations with two scaling factors  $A_{Load}$  and  $A_R$  are shown in Fig. 3(a). The comparison between the measured and the estimated voltage responsivity shows that without any fitting parameters, we obtain reasonable agreement. Indeed, the right order of magnitude of the responsivity and its main functional (versus  $V_{BE}$ ) dependence are well reproduced. The negative part

of the estimated responsivity is a direct consequence of the measured negative part of  $\Delta I_{BE}$  – see Fig. 2(a). This result is not fully understood until now and needs further analysis.

Presented above results show that one can estimate current and voltage responsivities using current voltage characteristics,  $A_{Load}$  and  $A_R$  scaling factors. One can observe also that  $A_R$  factor is the main factor that may reduce DHBT THz responsivities by orders of magnitude. Increasing the value of this factor (by reduction of  $C_{BE}$  capacitance) is the key point of DHBT THz responsivity improvement. This can be achieved for example by decreasing the HBTs emitter area.

#### IV. THz COMPUTED TOMOGRAPHY

To evaluate the usefulness of the InP DHBT detector we performed THz 3D imaging, with the 3-finger device having a maximum of detection at 322 GHz. THz computed tomography method is based on continuous THz sources. The 3D representations of the internal structure of the object are reconstructed using cross-sectional images from transmission measurements at different angles of incidence. Reconstructing the slices of a 3D tomographic image requires a certain number of projection measures. To obtain these projection measures, the object was placed on motorized stages moving in the plane perpendicular to the optical axis of the InP-based DHBT detector. The stages performed two translations along the horizontal (X) and vertical (Y) axes and a rotation around the vertical axis. Each projection measure depends on all of the attenuations that THz wave undergoes while passing through the object. A tomographic reconstruction consists of inverting a modeling of this dependence to reconstruct a discrete version of the attenuation coefficient map.<sup>20</sup>

The reconstruction proposed here is based on modeling the THz radiation propagation by a Gaussian beam. It took in account Gaussian intensity profile, beam waist and the shape of a THz beam while propagating in the air, and it assumed that the effects of both diffractions and reflections can be neglected.<sup>20</sup> Therefore, the acquisition modeling is linear and can be represented by a Radon matrix.<sup>21</sup> For each slice to be reconstructed, the Radon matrix is built by discretizing, for each position of the motorized stages, the Gaussian beam all along the optical axis. The reconstruction of the attenuation coefficients has been performed by using a maximum likelihood expectation maximization algorithm,<sup>22</sup> since the values to be reconstructed are positive by nature. The regularization is obtained by early stopping the iterative reconstruction process at the 20th iteration.<sup>23</sup> This iteration has been chosen since it provides a good tradeoff between resolution and number of artifacts in the reconstructed image.

This THz computed tomography experiment aims at showing the performance of imagers based on InP-DHBT detector technology to detect potentially dangerous objects. To mimic this situation, we have concealed a metallic blade in a plastic cylindrical box with plastic foil and pills (Fig. 4).

For this experiment, the translation step has been set to 0.2 mm and the rotation step has been set to 20° to comply with the required resolution. Subsequently, 400 slices with size 280 x 280 have been reconstructed based on 5040 projections measures acquired all around the object.

Fig. 5(a) shows a reordering of the projection measures for a given acquisition angular position to mimic a computed tomography-like 2D projection measure. At some angles, it was really hard to recognize the concealed object on a single 2D projection which only represents the sum of the attenuation values of all materials traversed by the collimated beam. Fig. 5(b) shows a projection, for the same angular position, of the reconstructed attenuation coefficient map. On Fig 5(a), one can



FIG. 4. The pillbox with pills, plastic foil and blade: (a) all elements outside, (b) inside.

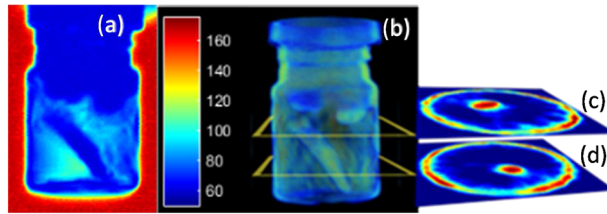


FIG. 5. (a) Projection measures, (b) projection of the reconstructed attenuation coefficient map, (c) and (d) two corresponding horizontal slices.



FIG. 6. Projection of the reconstructed pillbox where every low-attenuation coefficient voxels have been made transparent.

suspect the existence of the metallic blade, while this existence is more noticeable on Figs. 5(b), 5(c), and 5(d). Fig. 5(c) and 5(d) show two reconstructed slices. On both slices, the presence of an object having the density and the shape of a metallic blade is obvious.

Forging an image where the voxels whose attenuation coefficient is below a given threshold have been made transparent highlights this detection. The projection of such an image is presented in Fig. 6. The shape of the blade appears clearly in the center of the 3D image.

## V. CONCLUSIONS

In conclusion, we investigated InP DHBT as THz detectors. THz active imaging has been demonstrated by using DHBT detectors with commercial sub-THz source, allowing for high quality computed tomography based 3D imaging of concealed objects. We have shown that: i) the experimental THz voltage and current responsivities can be related to static current-voltage characteristics, ii) the further optimization needs especially improvement of the scaling factor  $A_R$  (by reduction of capacitance  $C_{BE}$ ), and iii) the high speed voltage responsivity needs additionally careful choice of the read-out circuit impedance to avoid parasitic loading effect losses. The last optimization is especially important for potential applications of InP DHBTs in THz wireless communication.

## ACKNOWLEDGMENTS

We are grateful to H. Zirath for helpful discussions concerning the modeling part of this work. This work was financially supported by the ANR project NADIA “Integrated NAno-Detectors for

terahertz Applications” (ANR-13-NANO-0008), by the financial support from ERA.NET RUS Plus through the project Terasens n° 149, and by the Region of Occitanie/Pyrénées-Méditerranée through the GEPETO “Terapole Platform”.

- <sup>1</sup> J.-Q. Lü and M. S. Shur, *Appl. Phys. Lett.* **78**, 2587 (2001).
- <sup>2</sup> Y. Kurita, G. Ducournau, D. Coquillat, A. Satou, K. Kobayashi, S. Boubanga Tombet, Y. Meziani, V. V. Popov, W. Knap, T. Suemitsu, and T. Otsuji, *Appl. Phys. Lett.* **104**, 251114 (2014).
- <sup>3</sup> E. Ojefors, U. R. Pfeiffer, A. Lisauskas, and H. G. Roskos, *IEEE J. Solid-State Circuits* **44**, 1968 (2009).
- <sup>4</sup> S. Blin, L. Tohme, D. Coquillat, S. Horiguchi, Y. Minamikata, S. Hisatake, P. Nouvel, T. Cohen, A. Penarier, F. Cano, L. Varani, W. Knap, and T. Nagatsuma, *J. of Communications and Networks* **15**, 559 (2013).
- <sup>5</sup> R. A. Hadi, J. Grzyb, B. Heinemann, and U. Pfeiffer, *IEEE Bipolar/BiCMOS Circuits and Technology Meeting* (2012).
- <sup>6</sup> V. Vassilev, H. Zirath, R. Kozhuharov, and S. Lai, *IEEE Transactions on Microwave Theory and Techniques* **61**, 2353 (2013).
- <sup>7</sup> D. Coquillat, V. Nodjiadjim, A. Konczykowska, N. Dyakonova, C. Consejo, S. Ruffenach, F. Teppe, M. Riet, A. Muraviev, A. Gutin, M. Shur, J. Godin, and W. Knap, *J. Phys.: Conf. Ser.* **647**, 012036 (2015).
- <sup>8</sup> D. Yong, J. Yun, J. Kim, K. Song, M. Kaynak, B. Tillack, and J.-S. Rieh, *Proc. 40th IRMMW-THz: Int. Conf. on Infrared, Millimeter, and Terahertz Waves, Hong-Kong, China* (2015).
- <sup>9</sup> W. Knap and M. Dyakonov *et al.*, *J. Infrared Millimeter Terahertz Waves* **30**, 1319 (2009).
- <sup>10</sup> W. Knap, S. Rummyantsev, M. Vitiello, D. Coquillat, S. Blin, N. Dyakonova, M. Shur, F. Teppe, A. Tredicucci, and T. Nagatsuma, *Nanotechnology* **24**, 214002 (2013).
- <sup>11</sup> V. Katopodis, C. Tsokos, D. de Felipe, M. Spyropoulou, A. Konczykowska, A. Aimone, P. Groumas, J.-Y. Dupuy, F. Jorge, H. Mardoyan, R. Rios-Müller, J. Renaudier, P. Jennevé, F. Boitier, A. Pagano, M. Quagliotti, D. Roccatto, T. K. Johansen, M. Tienforti, A. Vannucci, H.-G. Bach, N. Keil, H. Avramopoulos, Ch. Kouloumentas, and M. Riet, *Proc. SPIE* **10561**, 1056107 (2018).
- <sup>12</sup> J.-Y. Dupuy, A. Konczykowska, F. Jorge, M. Riet, P. Berdager, V. Nodjiadjim, J. Godin, and A. Ouslimani, *IEEE Transactions on Microwave Theory and Techniques* **61**, 517 (2013).
- <sup>13</sup> M. Sakowicz, J. Łusakowski, K. Karpierz, M. Grynberg, W. Knap, and W. Gwarek, *J. Appl. Phys.* **104**, 024519 (2008).
- <sup>14</sup> K. S. Yngvesson, *Microwave Semiconductor Devices* (Kluwer Academic Publishers, Norwell, MA, 1991).
- <sup>15</sup> A. G. Golenkov and F. F. Sizov, *Semiconductor Physics, Quantum Electronics & Optoelectronics* **19**, 129 (2016).
- <sup>16</sup> W. Stillman, M. S. Shur, D. Veksler, S. Rummyantsev, and F. Guarin, *Electron. Lett.* **43**, 422 (2007).
- <sup>17</sup> O. Klimenko, W. Knap, B. Iniguez, D. Coquillat, Y. Mityagin, F. Teppe, N. Dyakonova, H. Videlier, D. But, F. Lime, J. Marczewski, and K. Kucharski, *J. Appl. Phys.* **112**, 014506 (2012).
- <sup>18</sup> D. Coquillat, V. Nodjiadjim, S. Blin, A. Konczykowska, N. Dyakonova, C. Consejo, P. Nouvel, A. Pènarier, J. Torres, D. But, S. Ruffenach, F. Teppe, M. Riet, A. Muraviev, A. Gutin, M. Shur, and W. Knap, *Int. J. Hi. Spe. Ele. Syst.* **25**, 1640011 (2016).
- <sup>19</sup> D. Coquillat, J. Marczewski, P. Kopyt, N. Dyakonova, B. Giffard, and W. Knap, *Optics Express* **24**, 272 (2016).
- <sup>20</sup> B. Recur, J. P. Guillet, I. Manek-Hönniger, J. C. Delagnes, W. Benharbone, P. Desbarats, J. P. Domenger, L. Canioni, and P. Mounaix, *Optics Express* **20**, 5817 (2012).
- <sup>21</sup> C. L. Morgan, *Basic Principles of Computed Tomography* (University Park Press, Baltimore, 1983).
- <sup>22</sup> K. Lange and R. Carson, *J. Comput. Assist. Tomogr* **8**, 306 (1984).
- <sup>23</sup> H. E. Fleming, *Linear Algebra Appl.* **130**, 133 (1990).